Quadruple-band anisotropic perfect absorption and terahertz sensing in monolayer black phosphorus with flower-like air hole

Y. PAN*
School of Physics and Optoelectronic Engineering, Yangtze University, Jingzhou, 434023, China

We design and study a multi-band anisotropic black phosphorus (BP) based absorber. The proposed absorber is consisting of a monolayer black phosphorus, a crystalline silicon layer, and a gold substrate. Numerical results show that the absorber has four absorption peaks both close to perfect absorption, generated by critical coupling. Absorption can be adjusted by varying key parameters, such as semi-major axis, short-half axis, height, period, and the polarization angle. The sensitivity *S* of peak 1, peak 2, peak 3, and peak 4 are about 0.85 *THz/RIU*, 0.875 *THz/RIU*, 1.15 *THz/RIU*, and 1.05 *THz/RIU*, respectively. As well, the *FOMs* corresponding to resonance peak 1, peak 2, peak 3, and peak 4 are about 8.10 RIU^{-1}, 21.88 RIU^{-1}, 9.35 RIU^{-1}, and 20.25 RIU^{-1}, respectively. The proposed BP-based quadruple-band absorber provides a basis for designing borophene-based sensor and other electronic-photonics devices.

(Received September 15, 2023; accepted April 10, 2024)

Keywords: Black phosphorus, Critical coupling, Perfect plasmonic absorber

1. Introduction

Since ancient times, people have always had a great curiosity about light. With the progress of science and technology, people have a deeper understanding of light [1-4]. The proposal of metamaterial absorbers makes possible 100% absorption of light, and the perfect absorbers play an indispensable role in the frontier optical field. They can be used for plasma-enhanced [5,6], energy detection and conversion device [7-10], optical modulators [11], solar absorbers [12], plasmon introduce transparency [13-15],and sensors [16-18]. Among them, metamaterials are composite materials with artificially designed structures and show extraordinary physical properties that natural materials do not have, such as unique negative refraction [19], invisible [20], perfect lens [21], and perfect absorber [22]. So far, the existing proposed metamaterials can be applied in most of the microwave regions [23-29]. In recent years, two-dimensional materials have attracted much attention because of their high light absorption. Among them, graphene, hexagonal boron nitride (h-BN), molybdenum disulfide, black phosphorus, and other two-dimensional (2D) materials have become a hot research field because of their unique physical and chemical properties [30]. Black phosphorus (BP) [31,32], as an emerging 2D material, has attracted wide attention due to its unique physicochemical properties. Different from other isotropic two-dimensional materials such as graphene [33], the unique fold structure of black phosphorus enables it to present a particularly excellent property and be widely used.

To enhance the interaction between light and black phosphorus in the structure, many BP-based devices have been widely studied at THz frequencies. Among them, Xu et al. studied the coupling between BP and graphene plasma in the mid-infrared band [34]. Similarly, Zhang et al. studied that black phosphorus can achieve anisotropic perfect absorption under plasmon resonance excitation, with a maximum absorption rate of 99.56% [35]. Liu et al. studied the Fano resonance between BP and a gold ring [36]. However, most previous BP-based absorbers face problems such as narrow wavelength tuning range and single absorption band. How to design a new structure with a more intelligent response and flexible tenability is a huge challenge.

In this paper, we proposed an easily fabricated

structure which consisting of a monolayer black phosphorus, a silicon layer (with a flower-like air hole), and an Au gold substrate. Owing to the critical coupling to the guidance resonance. Four narrow absorption peaks are presented at 4.29 THz, 5.23 THz, 5.89 THz, and 6.72 THz, and the corresponding absorption rates are 99.61%, 99.76%, 99.42%, and 99.59%, respectively. However, due to the anisotropic nature of BP, for TM polarization, the absorption efficiencies are 84.53%, 80.27%, 99.70%, and 82.97% at 4.35 THz, 5.26 THz, 5.88 THz, and 6.73 THz, respectively. The influence of structural parameters (such as period, semi-major axis, short half axis, polarization angle, height, and refractive index) on the spectral absorption is investigated detail. The maximum refractive index sensitivity and FOM are calculated, and the results are 1.08*THz/RIU* and 21.88RIU^{-1}, respectively. The proposed BP-based narrow band absorber can find potential applications in the areas such as modulator, biosensors and photodetectors in terahertz band.

2. Model and theory

The proposed the schematic diagram of the proposed absorber is illustrated Fig. 1 (a). A monolayer black phosphorus is covered on the surface of the absorber. It consists of three parts: the top BP layer as a destructive material, a silicon layer, and a gold substrate as a metal mirror to inhibit the transmission. The periods in the x and y directions are P_x and P_y, respectively. The height of silicon layer is h and the thickness of the *Au* is *t*. As well, the flower-like air hole is consists of four rotationally intersecting elliptical holes. As shown in Fig. 1 (b), the angles between horizontally elliptical hole and extra holes are set to 45°, 90°, 135° in counter-clockwise direction, respectively. The semi-major axis of the elliptical hole is *a* and the short half axis is *b*. The structural parameters of the designed absorber are presented in Table 1. The refractive index of silicon is 3.42.

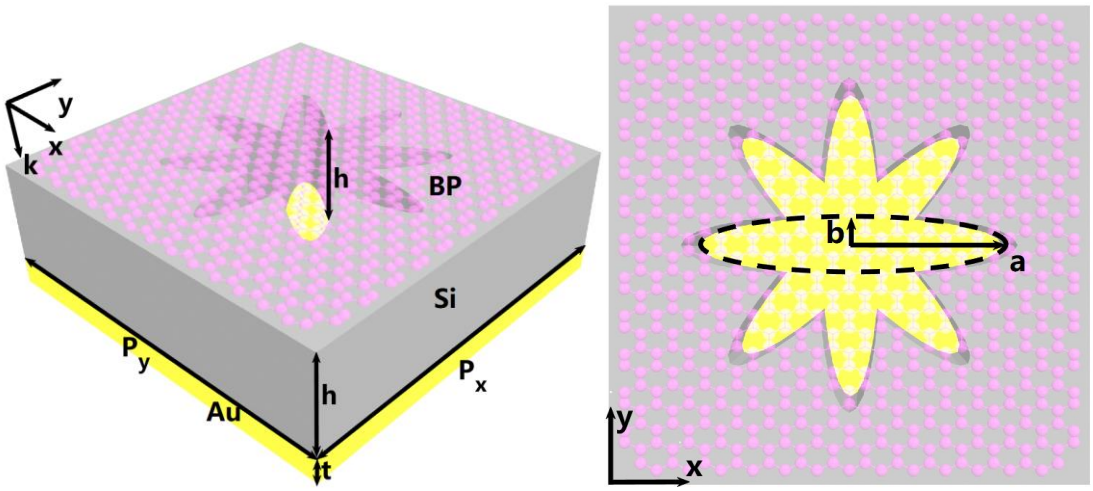

(a) *(b)*

Fig. 1. (a) Three dimension unit cell diagram of the proposed multi-band absorber. (b) The vertical view of the proposed absorber (color online)

Table 1. The structural parameters of the structure

Parameter	Symbol	Quantity	Unit
Period of the structure	$P_x = P_y$	30	μm
Thickness of the Si	h	8	μm
Thickness of the Au	t	1	μm
semi-major axis of the elliptical hole	a	10.5	μm
short half axis of the elliptical hole	b	2	μm

The optical properties of the monolayer black phosphorus can be described by an equivalent Drude model. Its surface conductivity can be expressed as [37]:

$$\sigma_j = \frac{iD_j}{\pi\left(\omega + i\frac{\eta}{\hbar}\right)} \tag{1}$$

$$D_j = \frac{\pi e^2 n_s}{m_j} \tag{2}$$

where j represents the orientation correlation which is taken to be x and y, and Dj is the Drude weight m_j stands for the effective mass in x and y directions, e and n_s represent the electron charge and free carrier density, respectively. The effective mass along the x and y direction can be expressed as:

$$m_x = \frac{\hbar^2}{\frac{2\gamma^2}{\Delta} + \eta_c} \tag{3}$$

$$m_y = \frac{\hbar^2}{2v_c} \tag{4}$$

For monolayer black phosphorus, $\gamma = \frac{4a}{\pi}$, $\Delta = 2eV$, $\eta_c = \frac{\hbar^2}{0.4m_0}$, $v_c = \frac{\hbar^2}{1.4m_0}$, a is the scale length of the BP and m_0 is the standard electronic mass. Here, η = 10meV, the electron doping of the monolayer BP material is set to: n_s=3×10 cm^{-2}, which remains unchanged unless specified.

It appears here that the difference between the effective mass along the x direction and the y direction is the main reason for the anisotropy of the black phosphorus. The dielectric function of the film (with a 2D conductivity) can be expressed as:

$$\varepsilon_j = \varepsilon_r + \frac{i\sigma_j}{\varepsilon_0 \omega a} \tag{5}$$

The relative dielectric constant of the single atomic layer black phosphorus at high frequency is $\varepsilon_r = 5.76$, and the characteristic size of the black phosphorus is a 0.22 nm. The electron doping concentration of black phosphorus can be changed by applying the bias voltage. Using the equivalent capacitance model, the relationship between the carrier concentration n_s in the film black phosphorus and the bias voltage V_{gate} can be expressed as [38]:

$$V_{gate} = V_{fb} + E_F - E_c(z=0) + \frac{q_0 n_s}{\varepsilon_0 \varepsilon_{ox}} t_{ox} \tag{6}$$

where $V_{fb} = 0V$ represents the flat band voltage, E_F represents the Fermi level, E_c is the conduction band level of black phosphorus, t_{ox} is the thickness of the dielectric layer, q_0 represents the quantity of electricity, ε_0 and ε_{ox} represent the dielectric constant of free space and the dielectric constant of the dielectric layer, respectively.

Lumerical FDTD software was used to build the model and simulate the absorption response between the incident electromagnetic wave and the proposed absorber [39]. Periodic boundary conditions are applied in the x and y directions, and perfectly matched layers (PMLs) are set in the z direction, to ensure accuracy, a 3D rectangular grid with the size of $0.2\mu m$ is used in the calculation region. The total simulation region is 30 μm ×30 μm × 3000 μm. A plane wave source with y-direction polarized (TE mode) is incident from the z-direction. The wavelength of the source is range from 3*THz* to 8 *THz*. Note that the incident light source is placed in the air with an ambient refractive index of n=1. The absorption spectrum of the configuration can be defined as A=1-T-R, where T and R indicate transmission and reflection, respectively. However, the reflection of the Au substrate seriously hinders the transmission, and the value of T is almost zero, so the absorption expression can be more simply expressed by A=1-R.

3. Result and discussion

The absorption spectrum is presented in Fig. 2 (a) under TE-polarized wave. It is clear to observe that the absorber possesses four nearly perfect absorption peaks. The absorption efficiencies are 99.61%, 99.76%, 99.42%, and 99.59% at 4.29 THz, 5.23 THz, 5.89 THz, and 6.72 THz, respectively.

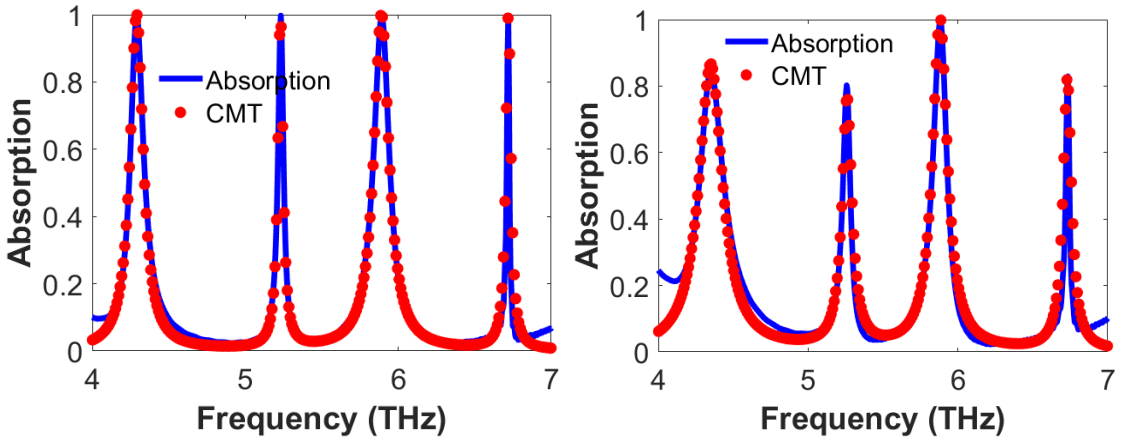

(a) *(b)*

Fig. 2. (a) The absorption of the proposed multi band absorber (blue solid line) under TE polarization, and the calculated absorption spectrum with CMT (red solid dots). (b) The absorption of the proposed multi band absorber (blue solid line) under TM polarization, and the calculated absorption spectrum with CMT (red solid dots) (color online)

The absorption behavior can be illustrated by the coupled-mode theory. The result of reflection coefficient is calculated by CMT, with a sufficient order of the Fourier expansion to ensure convergence. The algorithm has been tested on a series of absorption structures. For a single mode absorber, the time-dependent resonance amplitude a is described as [40]:

$$\frac{da}{dt} = (j\omega_0 - \delta - \gamma)a + \sqrt{2\gamma}S_+ \tag{7}$$

$$S_- = -S_+ + \sqrt{2\gamma}a \tag{8}$$

Among them, S_+ and S_- indicate as the amplitudes of input and outgoing wave, respectively. δ and γ are considered as intrinsic loss and external leakage rate. ω_0 is the resonance frequency of the absorber. Based on equations (7) and (8), the reflection coefficient is expressed as:

$$r = \frac{S_-}{S_+} = \frac{j(\omega - \omega_0) + \delta - \gamma}{j(\omega - \omega_0) + \delta + \gamma} \tag{9}$$

The absorption coefficient is depicted as:

$$A = 1 - |r|^2 = \frac{4\delta\gamma}{(\omega-\omega_0)^2+(\delta+\gamma)^2} \quad (10)$$

From formula (10), when the intrinsic loss is equal to the external leakage rate at resonance frequency ($\omega = \omega_0$), the critical coupling is achieved. Further, the perfect absorption is realized. For the multi-band structure, according to CMT, the absorption efficiency can be obtained by equation (11) [41]:

$$A = \sum_{i=1}^{n} \frac{4\delta_i\gamma_i}{(\omega-\omega_i)^2+(\delta_i+\gamma_i)^2} \quad (11)$$

where n = 4 is the number of absorption modes. Fig. 2 (a) presents the calculated absorption curve by CMT. It exhibits a good matching degree. The full width at half maximum (FWHM) of four peaks are Δf = 0.105*THz*, Δf = 0.04*THz*, Δf = 0.123*THz*, Δf = 0.04*THz*, indicating that the line width of spectral absorption is very narrow. Then the quality factors are calculated by $Q_i = \frac{f_i}{\Delta f}$. As well, the theoretical quality factors are calculated by $Q_{CMT} = \frac{Q_\delta \cdot Q_\gamma}{(Q_\delta + Q_\gamma)}$. Here, the intrinsic loss and external leakage of the resonant mode can be defined as $Q_\delta = \frac{\omega_0}{2\delta}$ and $Q_\gamma = \frac{\omega_0}{2\gamma}$, respectively. The Q_1 of first peak is 40.86 and the corresponding Q_{CMT} is 41.25. The Q_2 of the second peak is 130.75 and the corresponding Q_{CMT} is 130.75, too. The Q_3 of the third peak is 47.89 and the corresponding Q_{CMT} is 49.08. The Q_4 and the corresponding Q_{CMT} of the fourth peak have a same result 168. The Q_i and Q_{CMT} are nearly identical, indicating that the total absorption of the absorber can be attributed to critical coupling. Similarly, the absorption spectrum under TM-polarized wave and the calculated curve is depicted in Fig. 2 (b). Obviously, the absorption spectrum exhibits significant polarization dependent characteristics due to the anisotropic properties of BP. The absorption efficiencies are 84.53%, 80.27%, 99.70%, and 82.97% at 4.35 THz, 5.26 THz, 5.88 THz, and 6.73 THz, respectively. All resonance frequencies exhibit varying degrees of blue shift. In the same way, we calculate and depict the fitting curve by CMT. It can be observed that the system changes from a critical coupling to an under coupling, which is characterized by $\delta > \gamma$. It is noted that there is a slight deviation between the CMT model and the FDTD simulation at a position away from the wavelength of the resonance, because the CMT assumes that there is no loss away from the resonance.

To obtain further insight into the physical mechanism of the enhanced light absorption effect, Fig.3 presents the simulated magnetic field distributions under TE-polarized wave. One can clearly see that the guided resonance with field confinement is mainly distributed in the lossless Si layer. The Au substrate can completely suppress transmission, so when the system satisfies the critical coupling, the localized incident energy at resonance can be fully absorbed by the system.

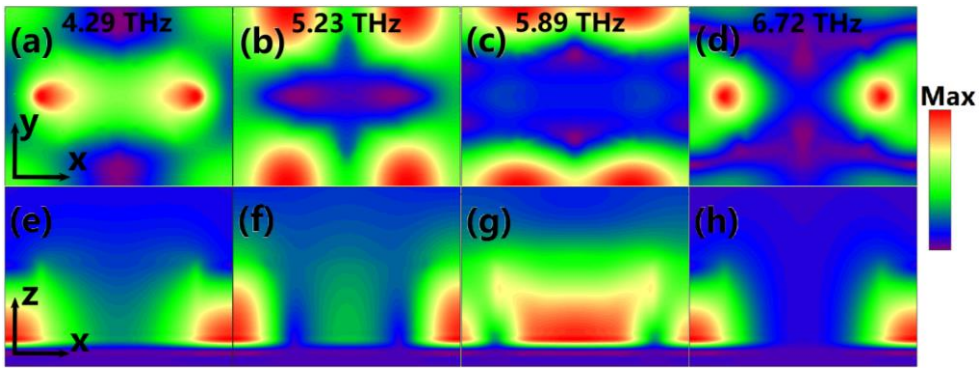

Fig. 3. The field distribution of the four resonant modes. (a)-(d): magnetic-field distributions in the x-y plane; (e)-(h): magnetic-field distributions in the x-z plane at different frequencies (color online)

At 4.29 *THz* and 6.72 *THz*, we can observe that the energies are confined at the horizontal air hole. At 5.23 *THz* and 5.89 *THz*, the magnetic field distributions are located at the edges of vertical flower-like aperture. The maximum value of magnetic field intensity about the first peak is 0.018 A/m. The maximum value of magnetic field intensity about another peaks is 0.035 A/m. Therefore, the perfect absorption of first peak is originated form the Fabry-Perot resonance [42]. The perfect absorption of second and third peaks are originated form the strong magnetic resonance [43]. The perfect absorption of forth peak is originated form the interaction between strong magnetic resonance and Fabry-Perot resonance.

Furthermore, although the structure is centrally rotationally symmetric, this BP-based absorber exhibits polarization dependent features due to the anisotropy of BP, as shown in Fig.4. (a) and (b).

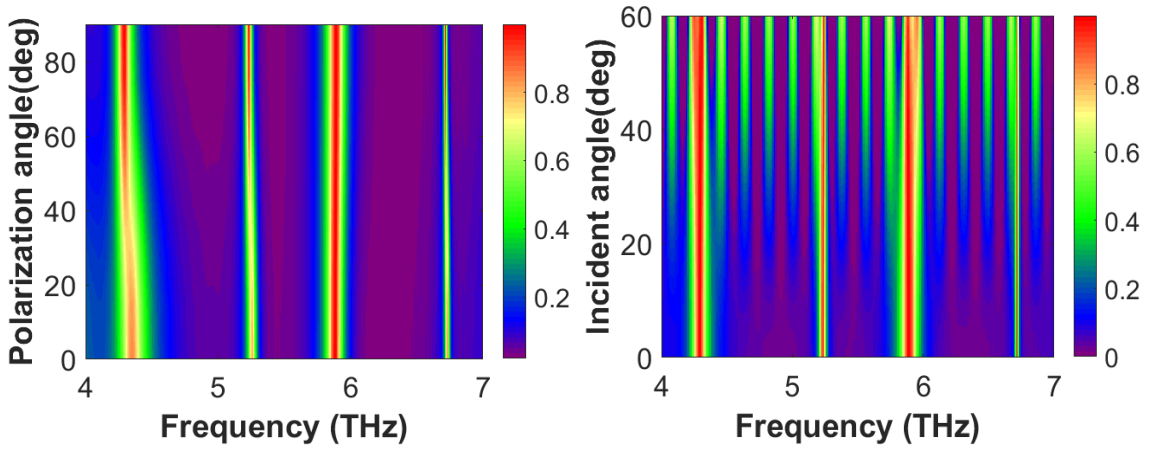

Fig. 4. (a) The relationship between absorption spectra and different polarization angles; (b) The relationship between absorption spectra and different incident angles (color online)

When the polarization angle is declined from the 90° to 0°, the absorptivity decreases, the bandwidth increases slightly, and the absorption peaks exhibit slight blue-shift. When the incident angle is less than 40°, the sensor can maintain a higher absorption efficiency. It can meet practical requirements.

Subsequently, the influence of geometric parameters on the absorption performance is investigated. The absorption spectra under TE polarization conditions with different parameters are shown in Fig 5. The absorption variation of the semi-major axis a is depicted. With a increasing from 8.5 μm to 10.5 μm, the resonance frequencies exhibit varying degrees of blue shift. The absorption has been increased when a = 10.5 μm. Similarly, when the short half axis b increases from 1 μm to 3 μm with a step of 1 μm, the first absorption peak shifts from 4.22 THz to 4.34 THz, and the second absorption peak shifts from 5.07 THz to 5.38 THz, the third absorption peak shifts from 5.67 THz to 6.02 THz, the fourth absorption peak shifts from 6.57 THz to 6.78 THz. Fig. 5 (c) depicts the relationship between the absorbance and the silicon layer thickness (h). When h is increased from 7 μm to 9 μm with a step size of 1 μm, the first absorption peak is red-shifted from 4.56 THz to 4.09 THz, the second absorption peak shifts from 5.48 THz to 5.05 THz, the third absorption peak shifts from 6.23 THz to 5.64 THz, and the fourth absorption peak shifts from 6.89 THz to 6.59 THz,the position of the two absorption peaks can be adjusted by varying the thickness of the silicon layer. Fig. 5 (d) exhibits the absorption spectrum as a function of frequency and period (p). When p increases from 29 m to 31 μm, the first absorption peak is red-shifted from 4.41 THz to 4.19 THz, the second absorption peak shifts from 5.39 THz to 5.09 THz, the third absorption peak shifts from 6.09 THz to 5.72 THz, and the fourth absorption peak shifts from 6.93 THz to 6.52 THz. The reason for the red shift of the peaks is that the effective refractive index of the silicon layer increases with increasing period and thickness. Therefore, the absorber performance can be adjusted by changing the structural parameters, which is important for practical applications.

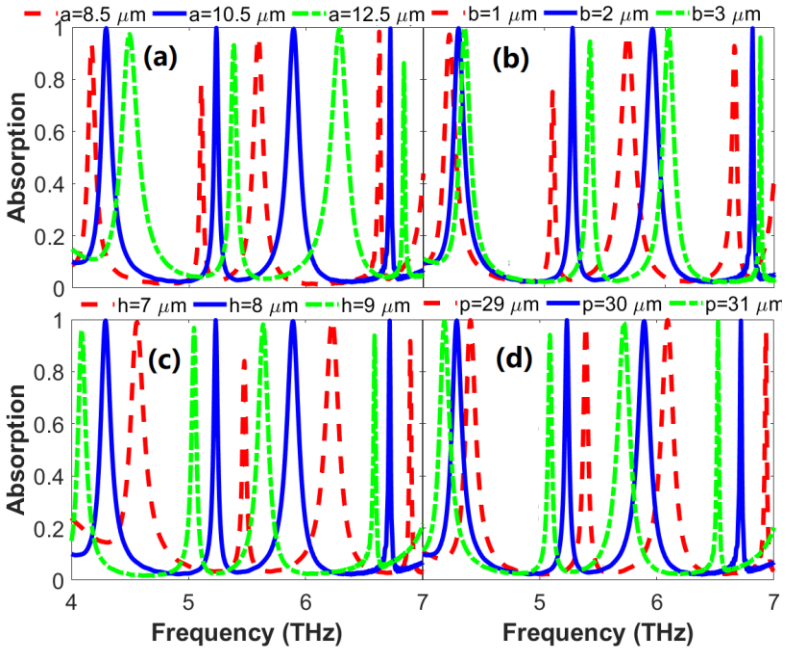

Fig. 5. Absorption response for the proposed absorber at different structural parameters under vertical illumination with TE-polarization: (a) a is allowed to change; (b) b is allowed to change; (c) h is allowed to change; (d) p is allowed to change. Except as indicated, the geometric parameters are fixed to the default values (color online)

Moreover, the relationship between background index and absorption spectra is presented in Fig. 6 (a). The increase of refractive index reduces the frequency of the resonance peaks. When the refractive index of the filling medium increases from 1 to 1.2, the position of the resonance peak is significantly red-shifted, the first resonance frequency red-shifts from 4.29 THz to 4.12 THz, the absorption rate remains above 99%, the second resonance frequency red-shifts from 5.23 THz to 5.06 THz, the third resonance frequency red-shifts from 5.89 THz to 5.66THz, and the fourth resonance frequency red-shifts from 6.72 THz to 6.50 THz.

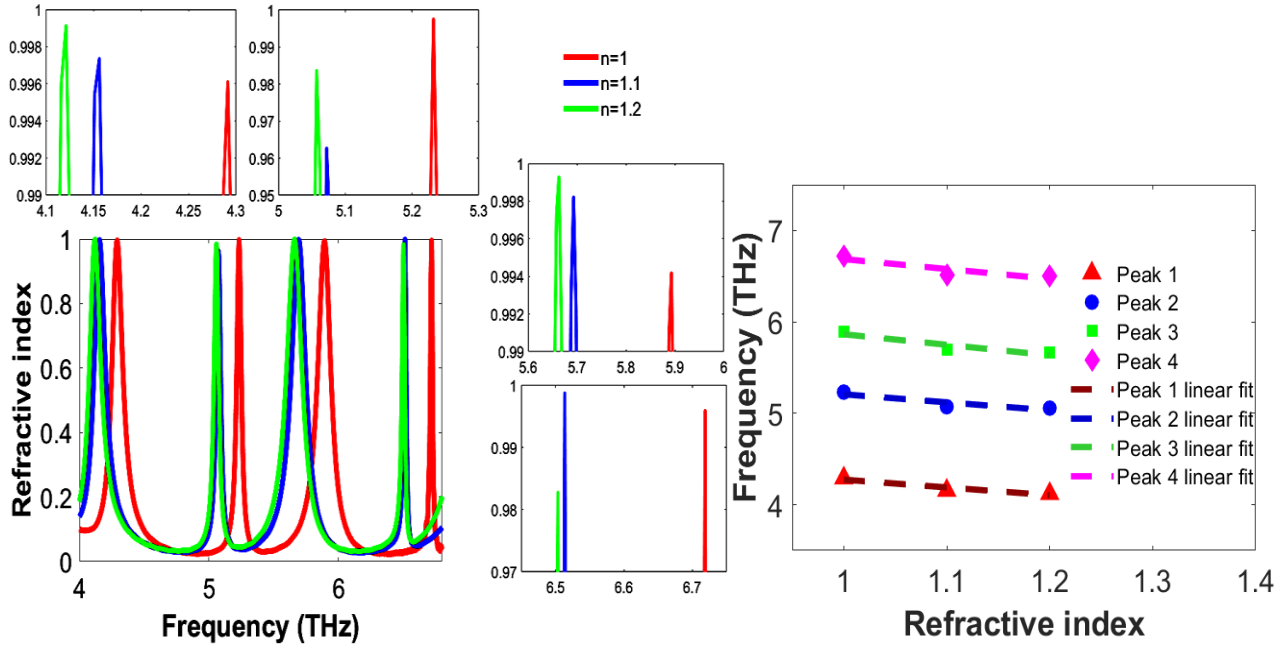

(a) *(b)*

Fig.6. (a) The absorption spectra with different refractive indices of the proposed structure; (b) The relationship between the refractive indices and the resonant frequencies (color online)

These results show that the proposed BP-based structure has the potential for terahertz sensing. The sensing capability of the sensor is usually estimated by the sensitivity (S) and figure of merits (FOM).

$$S = \frac{\Delta f}{\Delta n} \tag{12}$$

$$FOM = \frac{S}{FWHM} \tag{13}$$

where Δf is the spectral shift caused by the refractive index of the surrounding environment and Δn is the change of the refractive index. The proposed BP THz tunable sensor has four channels, and the linear fit sensitivity S for peak 1, peak 2, peak 3, and peak 4 are 0.85 *THz/RIU*, 0.875 *THz/RIU*, 1.15 *THz/RIU*, and 1.05 *THz/RIU*, respectively. As shown in Fig. 6 (b), the *FOMs* corresponding to resonance peak 1, peak 2, peak 3, and peak 4 are 8.10 RIU^{-1}, 21.88 RIU^{-1}, 9.35 RIU^{-1}, and 20.25 RIU^{-1}, respectively. It is worth mentioning that, compared with the work, the proposed BP-based multi narrow band absorber possesses a narrow line width, a higher absorption rate, and a bigger sensitivity. The sensing performance of other related structures is compared and the results are shown in Table 2. The sensitivity of the present the proposed BP-based double narrow band absorber is relatively good compared to previous work [44-48].

Table 2. Comparisons between the proposed absorber and other works

Reference	Year	Max-Sensitivity (THz/RIU)	Max-FOM (RIU−1)	Max-Peak Absorption(%)
[44]	2022	0.19	/	98.0
[45]	2015	1.19	6.56	99.0
[46]	2021	0.85	3.16	99.8
[47]	2015	2.37	179.95	99.8
[48]	2022	4.72	13.88	99.0
This work	2023	1.08	21.88	99.76

Next, we investigate the absorption spectrum with different electron doping n_s. As shown in Fig. 7 (a), for TE polarization, as n_s increases from n_s = $1\times10^{13}cm^{-2}$, n_s = $3\times10^{13}cm^{-2}$ to n_s = $5\times10^{13}cm^{-2}$, the four resonance peaks show a blue shift, and the absorption rate is increased to unity and then decreased. This is because the real part of the effective refractive index of BP decreases with increasing electron concentration, while the imaginary part of the effective refractive index of BP increases with increasing electron concentration. For TM polarization, similar phenomena can be observed in Fig. 7 (b).

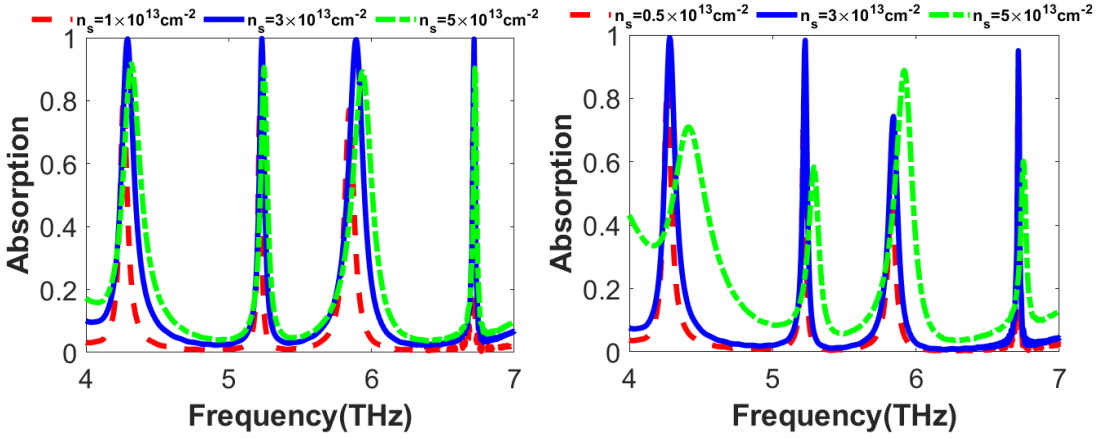

(a) *(b)*

Fig. 7. (a) FDTD simulated absorption spectra at $n_s = 1\times10^{13}cm^{-2}(red)$ $n_s = 3\times10^{13}cm^{-2}(blue)$, *and* $n_s = 5\times10^{13}cm^{-2}(green)$ *under TE-polarized wave. (b) FDTD simulated absorption spectra at* $n_s = 1\times10^{13}cm^{-2}(red)$, $n_s = 3\times10^{13}cm^{-2}(blue)$, *and* $n_s = 5\times10^{13}cm^{-2}(green)$ *under TM-polarized wave (color online)*

As n_s determines the refractive index of BP, as n_s increases from $n_s = 0.5\times10^{13} cm^{-2}$ to $n_s = 5\times10^{13} cm^{-2}$, the coupling of the system is changed from over coupling to under coupling, the absorption rate in both cases is not perfect. When $n_s = 1\times10^{13} cm^{-2}$, critical coupling occurs, since the effective impedance of the structure matches with the free space at the two resonance frequencies.

4. Conclusion

We numerically proposed a tunable BP-based absorber to enhance the light absorption at THz frequencies. The absorber includes a revolving cross-air hole in a silicon layer covered with black phosphorus and Au substrate. The TE wave produces four nearly perfect absorption peaks at the incidence angle of $\theta = 0$. Due to the anisotropy of BP, the absorber exhibits polarization-dependent features. Moreover, the maximum sensitivity of the proposed absorber can be as high as 0.85 *THz/RIU*, 0.875 *THz/RIU*, 1.15 *THz/RIU*, and 1.05 *THz/RIU*. Such easy-to-fabricate structures may provide potential applications in many promising applications, such as optoelectronic detection, optical sensing, and other BP-based optoelectronic devices.

Acknowledgements

Supported by Yangtze Fund for college students' innovation and entrepreneurship (Grant No. Yz2022278).

References

[1] J. Liu, Y. Peng, B. Zhu, Y. Li, L. Zhang, J. Yu, Sensors and Actuators B: Chemical **357**, 131366 (2022).

[2] Y. Gu, B. Guo, Z. Yi, X. Wu, J. Zhang, H. Yang, Colloids and Surfaces A: Physicochemical and Engineering Aspects **653**, 129908 (2022).

[3] T. Cheng, H. Gao, G. Liu, Z. Pu, S. Wang, Z. Yi, H. Yang, Colloids and Surfaces A: Physicochemical and Engineering Aspects **633**, 127918 (2022).

[4] A. N. Emam, A. A. Mostafa, M. B. Mohamed, A. S. Gadallah, M. El-Kemary, Journal of Luminescence **200**, 287 (2018).

[5] F. Zhao, J. Lin, Z. Lei, Z. Yi, F. Qin, J. Zhang, P. Wu, Physical Chemistry Chemical Physics **24**(8), 4871 (2022).

[6] X. Q. Zhang, X. W. Xia, J. P. Xu, M. T. Cheng, Y. P. Yang, Chinese Physics B **28**(11), 114207 (2019).

[7] H. Xiong, X. Ma, B. Wang, H. Zhang, Sensors and Actuators A: Physical **366**, 114972 (2024).

[8] H. Xiong, X. Ma, H. Liu, D. Xiao, H. Zhang, Applied Physics Letters **123**(15), 153902 (2023).

[9] Q. Yang, H. Xiong, J. Deng, B. Wang, W. Peng, H. Zhang, Applied Physics Letters **122**(25), 253901 (2023).

[10] J. Deng, H. Xiong, Q. Yang, M. Suo, J. Xie, H. Zhang, IEEE Sensors Journal **23**(19), 22459 (2023).

[11] J. Jiang, Y. Xu, Y. Li, L. Ren, F. Chen, S. Cheng, X. Zhou, Optik **246**, 167855 (2021)

[12] X. Liu, T. Starr, A. F. Starr, W. J. Padilla, Physical Review Letters **104**(20), 207403 (2010).

[13] B. Wang, G. Duan, W. Lv, Y. Tao, H. Xiong, D. Zhang, G. Yang, F. Shu, Nanoscale **15**(45), 18435 (2023).

[14] B. Wang, Q. Zeng, S. Xiao, C. Xu, L. Xiong, H. Lv, J. Du, H. Yu, Journal of Physics D: Applied Physics **50**(45), 455107 (2017).

[15] B. Wang, J. Yang, Q. Zeng, G. Li, H. Yu, F. Chen, C. Yu, T. Wang, Physica Scripta **98**(12), 125525 (2023).

[16] C. Liu, H. Li, H. Xu, M. Zhao, C. Xiong, M. Li, K. Wu, New Journal of Physics **22**(7), 073049 (2020).

[17] X. Wu, Y. Zheng, Y. Luo, J. Zhang, Z. Yi, X. Wu, P. Wu, Physical Chemistry Chemical Physics **23**(47), 26864 (2021).

[18] R. A. Shelby, D. R. Smith, S. Schultz, Science **292**(5514), 77 (2001).

[19] H. F. Ma, T. J. Cui, Nature communications **1**(1), 21 (2010).

[20] J. B. Pendry, Physical Review Letters **85**(18),

3966 (2000).
[21] N. I. Landy, S. Sajuyigbe, J. J. Mock, D. R. Smith, W. J. Padilla, Physical Review Letters **100**(20), 207402 (2008).
[22] J. Hao, L. Zhou, M. Qiu, Physical Review B **83**(16), 165107 (2011).
[23] X. Liu, T. Tyler, T. Starr, A. F. Starr, N. M. Jokerst, W. J. Padilla, Physical Review Letters **107**(4), 045901 (2011).
[24] T. J. Cui, S. Liu, L. L. Li, Light: Science and Applications **5**(11), e16172 (2016).
[25] S. Liu, T. J. Cui, Q. Xu, D. Bao, L. Du, X. Wan, Q. Cheng, Light: Science Applications **5**(5), e16076 (2016).
[26] S. Liu, L. Zhang, Q. L. Yang, Q. Xu, Y. Yang, A. Noor, T. J. Cui, Advanced Optical Materials **4**(12), 1965 (2016).
[27] T. J. Cui, Journal of Optics **19**(8), 084004 (2017).
[28] T. J. Cui, National Science Review **5**(2), 134 (2018).
[29] W. Wang, Y. Li, F. Chen, Physical Chemistry Chemical Physics **25**(35), 23855 (2023).
[30] H. Yan, X. Li, B. Chandra, G. Tulevski, Y. Wu, M. Freitag, F. Xia, Nature Nanotechnology **7**(5), 330 (2012).
[31] X. Wang, A. M. Jones, K. L. Seyler, V. Tran, Y. Jia, H. Zhao, F. Xia, Nature Nanotechnology **10**(6), 517 (2015).
[32] Y. Zhu, S. Murali, W. Cai, X. Li, J. W. Suk, J. R. Potts, R. S. Ruoff, Advanced Materials **22**(35), 3906 (2010).
[33] A. Vakil, N. Engheta, Science **332**(6035), 1291 (2011).
[34] Y. Huang, Y. Liu, Y. Shao, G. Han, J. Zhang, Y. Hao, Nanomaterials **11**(6), 1442 (2021).
[35] F. Chen, H. Zhang, L. Sun, J. Li, C. Yu, Optics and Laser Technology **116**, 293 (2019).
[36] Z. Liu, K. Aydin, Nano letters **16**(6), 3457 (2016).
[37] Khalilzadeh Hamed, Amir Habibzadeh-Sharif, Niloufar Anvarhaghighi, J. Opt. Soc. Am. B **38**(12), 3920 (2021).
[38] M. R. Rakhshani, Plasmonics **15**(6), 2071 (2020).
[39] https://www.lumerical.com or https://www.novadownloads.com.
[40] Alipour Abbas, Ali Mir, Ali Farmani, Optics and Laser Technology **127**, 106201 (2020).
[41] Yue Lisha, Optics Express **29**(9), 13563 (2021).
[42] Y. Pan, Y. Li, F. Chen, J. Opt. Soc. Am. B **40**(12), 3057 (2023).
[43] Y. Pan, Y. Li, F. Chen, Plasmonics **19**(1), 193-20 (2023).
[44] M. Chen, Z. Xiao, Diamond and Related Materials **124**, 108935 (2022).
[45] Y. Zhang, T. Li, B. Zeng, H. Zhang, H. Lv, X. Huang, A. K. A. Azad, Nanoscale **7**(29), 12682 (2015).
[46] M. R. Nickpay, M. Danaie, A. Shahzadi, Plasmonics **17**(1), 237 (2021).
[47] S. Ma, P. Zhang, X. Mi, H. Zhao, Optics Communications **528**, 129021 (2023).
[48] M. Karthikeyan, P. Jayabala, S. Ramachandran, S. S. Dhanabalan, T. Sivanesan, M. Ponnusamy, Nanomaterials **12**(15), 2693 (2022).

*Corresponding author: yizhaopan@126.com